

Microstructural Evolution of a Hot-Stamped Boron Steel Automotive Part and Its Influence on Corrosion Properties and Tempering Behavior

Tiago N. Lima^a , Bruna Callegari^a , Luís Fernando Folle^a , Ygor Tadeu B. dos Santos^a ,
Luiz Gustavo Zamorano^{b,c}, Bruno Caetano dos S. Silva^a and Rodrigo Santiago Coelho^{a,b,*} 

^aSENAI CIMATEC, Instituto SENAI de Inovação em Conformação e União de Materiais (ISI-C&UM),
Av. Orlando Gomes, 1845, 41650-010, Salvador, BA, Brasil.

^bCentro Universitário SENAI CIMATEC, Programa de Pós-Graduação MPDS/GETEC/MCTI, Av.
Orlando Gomes, 1845, 41650-010, Salvador, BA, Brasil.

^cFORD Motor Company Brasil, Av. Henry Ford, 2000, 42810-225, Camaçari, BA, Brasil.

Received: November 21, 2022; Revised: March 16, 2023; Accepted: April 26, 2023

Boron-manganese steel 22MnB5 is extensively used in structural automotive components. Knowledge about its microstructural evolution during hot stamping and resistance spot welding (RSW) is extremely relevant to guarantee compliance with application requirements. Particularly, corrosion properties are critical to the application of uncoated sheet steels. However, microstructural studies are usually simplified to top-hat geometries, which might not be fully representative of the complex thermomechanical cycles locally faced by a real component. Therefore, the present work brings an extensive characterization of a hot-stamped 22MnB5 automotive B-pillar in terms of microstructure, hardness and corrosion resistance, which were correlated with a reverse engineering of the process using numerical simulation. Physical simulations of the subcritical heat affected zone (SCHAZ) of RSW were done to assess the influence of microstructure on martensite tempering. Results showed that the component undergoes a complex strain distribution along its body during hot stamping. Most heavily strained regions presented higher amounts of ferrite, leading to poorer corrosion resistance, since ferrite behaves as an anode. Physical simulations of the SCHAZ showed that the softening degree due to martensite tempering is solely affected by peak temperature, while other microstructural features appear to exert negligible or no influence.

Keywords: Hot stamping, resistance spot welding, 22MnB5, microstructure, simulation, corrosion.

1. Introduction

Advanced high strength steels (AHSS) have been increasingly used in recent years by the automotive industry, mainly due to demands for weight reduction in car body structures, aiming at energy saving and cost reduction, while still providing safety to passengers, with adequate levels of mechanical strength and toughness¹. Boron-manganese steels, such as 22MnB5, readily fulfil these requirements after hot stamping, a process in which the material is easily formed into complex-shaped parts in a ductile, austenitic condition and subsequently quenched, thus achieving a final martensitic microstructure. Currently, hot-stamped 22MnB5 is used in automotive components such as A and B-pillar reinforcements, bumper and door beams, front, rear and roof rails, and side-cross members².

Before hot stamping, 22MnB5 steel consists of a ferrite-pearlite microstructure with strength levels around 600 MPa, which increases to 1500 MPa in the martensitic condition attained upon processing³. However, due to the variation of deformation and heat extraction conditions along the intricate geometry of these components, certain regions can face incomplete martensitic transformation

or strain-induced ferritic and bainitic transformations, presenting complex microstructures consisting in mixtures of martensite, bainite and/or ferrite. Such microstructural complexity has been somewhat addressed in works usually involving hot tensile testing at different temperatures, in attempts to understand the effects of thermomechanical parameters on phase evolution^{4,5}. Even studies focused on machine learning approaches to predict such microstructure have been recently developed⁶.

Existing studies on the microstructural evolution of boron-manganese steels during hot stamping itself, as the ones by Naderi et al.⁷, Taylor and McCulloch⁸, and Grydin et al.⁹, usually rely on the simplified top-hat part geometry. In these studies, trends observed included higher hardness in radii regions, while side wall regions were softer. Results were correlated with differences in strain levels, part-die thermal contact and consequent cooling rate in different regions. Predominantly martensitic microstructures were observed in flat (non-deformed) regions of the component, where high thermal (conductive) contact was established between part and die. In contrast, a significant volume fraction of bainite was found in deformed regions, where limited thermal contact took place. With respect to deformation

*e-mail: rodrigo.coelho@fieb.org.br

effects, some investigations have shown that, in hot-stamped 22MnB5 boron steel, ferrite and bainite formation and retardation of martensitic transformation are favored by plastic deformation¹⁰.

After the stamping process, parts need to be joined to build the final car body. The most commonly used joining process in the automotive industry is resistance spot welding (RSW). However, during welding, the material faces thermal cycles that lead to significant microstructural changes in the heat affected zone (HAZ)¹¹. Shi et al.¹² observed that these changes might cause degradation and premature failure of the welded parts, with crack nucleation in the HAZ region. Lu et al.¹³ reported that boron steels in the hot-stamped condition undergo severe softening due to martensitic tempering that takes place in the HAZ sub-region known as subcritical heat affected zone (SCHAZ) during RSW. In this region, where the material reaches sufficiently high temperatures below A_{c1} , meaning that no ferrite or austenite forms, a significant reduction in hardness takes place because of this martensitic tempering, during which martensite suffers from carbon depletion.

The form how microstructure evolves during stamping and welding affects not only mechanical properties, but also corrosion resistance. In this regard, it is extremely relevant to understand how corrosion behavior of the steel correlates with microstructure, since a tendency exists in the automotive sector to increase the use of uncoated sheet steels in the near future, focusing on cost reduction and process simplification¹⁴. Currently, these materials are employed mostly with an Al-Si coating, which prevents surface oxidation and decarburization during hot stamping, in addition to enhancing corrosion resistance during use^{15,16}. Therefore, the application of steels without the protective coating requires an adequate understanding of how this interaction between microstructure and corrosion takes place, to avoid issues both during manufacturing and application. In multiphase steels, for example, Neetu et al.¹⁷ showed that ferrite behaves as an anode, meaning that its concentration in the microstructure decreases the corrosion resistance of steels, while microstructures containing higher fractions of bainite, pearlite and austenite present better corrosion resistance. Moon et al.¹⁸ reached the same conclusions regarding bainitic vs. ferritic microstructures. Besides, Inam et al.¹⁹ observed that, in martensitic steels, corrosion rates increase as the size of martensitic laths/needles decreases, due to a higher attack area. Zhao et al.²⁰ concluded that number, size, and distribution of phases, as well as grain size, can affect corrosion resistance.

To our best knowledge, there is no study available in which such evolution in real hot stamping conditions has been assessed, correlating thermal and deformation histories along the part's body with the resulting microstructure. Moreover, no knowledge exists about studies correlating such microstructure with aspects as corrosion resistance and martensitic tempering behavior. Existing studies evaluated only

specific aspects of the process, usually limited to laboratory-scale simulation of the process, such as: uniaxial hot tensile tests to evaluate formability and phase transformations in hot stamping conditions²¹⁻²⁴; top-hat or U- shaped part stamping for microstructure and hardness assessment^{7-9,25}; numerical simulation to validate deep learning as a tool to predict microstructure⁶; evaluation of the effect of transfer time on microstructure²⁶; and physical simulation of heat-affected zones, including SCHAZ softening²⁷⁻²⁹. Motivated by the presented context, the aim of this paper was to evaluate the microstructural distribution in a hot-stamped 22MnB5 automotive B-pillar and its influence on hardness and corrosion behavior. A reverse engineering approach using finite element analysis was used to derive strain and temperature distributions during the hot stamping process, for correlation with experimental results. Finally, the response of the microstructure in locations of interest to the thermal cycle that takes place in the SCHAZ during RSW was evaluated by physical simulations. The final goal is to provide a deeper understanding of the effects of different stages of manufacturing of sheet metal-based automotive parts on its microstructure, properties and performance.

2. Materials and Methods

2.1. Material

The hot-stamped B-pillars were provided by the company Magna Cosma (Camaçari, Bahia, Brazil). However, the components were fabricated elsewhere. The composition of their constituting 22MnB5 steel, obtained by inductively coupled plasma optical emission spectroscopy (ICP-OES) in a Foundry-Master Pro spectrometer, is shown in Table 1. Prior to the analysis, the Al-Si coating was mechanically removed from the part's surface with a 180-grit sandpaper.

The part's thickness, measured in different regions with the aid of a caliper, ranged between 1.04 and 1.12 mm, and its length was around 1250 mm. The as-received B-pillar, with the indication of positions from which samples for subsequent analyses were taken, is shown in Figure 1. Eighteen (18) spots were chosen along the pillar's body. They were divided into four groups, according to the part's feature in which they were located:

- Side wall: samples 01, 06, 13, 16, 18;
- Flange: samples 02, 03, 04, 07, 08, 12, 17;
- Top: samples 05, 09, 15;
- Radius (either top or bottom): samples 10, 11, 14.

2.2. Numerical simulation

In order to verify the hot stamping conditions in which the B-pillar was manufactured, numerical simulations were performed using the Simufact Forming software. These analyses were carried out to correlate the results of a reverse engineering approach with the most likely distribution of strain and cooling rates along the workpiece during the

Table 1. Composition of the 22MnB5 steel from the studied B-pillars (balance: Fe).

Element	C	Mn	Si	Al	Cr	Ti	Nb	Cu	Ni	B	P	S
wt%	0.24	1.15	0.26	0.038	0.20	0.034	0.005	0.01	0.001	0.003	0.022	<0.001

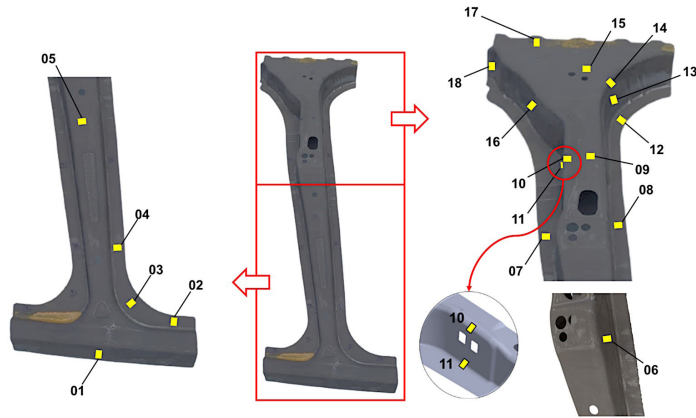


Figure 1. Analyzed B-pillar with indication of the positions from where samples were taken (side wall: samples 01, 06, 13, 16, 18; flange: samples 02, 03, 04, 07, 08, 12, 17; top: samples 05, 09, 15; radius: samples 10, 11, 14).

forming process. The sheet thickness used for simulations was of 1.1 mm. It was defined based on the thickness measurement in region 17, as this region presented almost zero deformation according to the simulation.

2.2.1. Tool geometry

The geometry of the B-pillar was collected from the final shape of the workpiece as part of the reverse engineering process to redesign tool details. The final computer-aided design (CAD) model is presented in Figure 2. As the hot stamping parameters were not provided for the analysis, boundary conditions were obtained from the works by Cui et al.³⁰, Hu et al.³¹, Park et al.³², and Wang and Ma³³, as will be specified ahead, in which the hot stamping of similar geometries made from the same material was studied, and from practical knowledge on industrial hot forming processes. The tools were designed with a constant 1.1 mm thick offset across the geometry. This is generally not recommended due to gaps resulting from thickness changes. Nonetheless, for hot stamping, as full contact is better for heat transfer, no gaps were used and this was observed by almost completely maintaining the original thicknesses through measurements on the final part. After creating the CAD model for the B-pillar workpiece, the next step was to redesign the tool, including all parts of the manufacturing process – punch, blank-holder and die – as shown in Figure 3.

Regarding the blank, it is typically cut to a shape that requires minimal trimming work after the forming process, especially if the process takes place at high temperature, mainly because the material after closed-die heat treatment will have such a high hardness that punch cutting would result in extensive tool wear. Thus, for this study, the blank was designed with a near-net shape. Clearly, there will still be some material removal in the final workpiece, as it would not be possible to form certain regions without extra material. This removal is usually done by laser cutting and time-consuming. Figure 4a shows the geometry adopted from the blank for the simulation, and Figure 4b shows that the geometry used for the simulation is suitable for the curved shape of the tools, as this saves time during the simulation and does not add too much strain to the blank.



Figure 2. CAD drawing of the B-pillar workpiece.

Figure 4c shows how the blank is positioned on the blank-holder and Figure 4d shows how the blank is positioned relative to the punch.

2.2.2. Boundary conditions

Simufact software offers three types of die models: rigid die without heat conduction, rigid die with heat conduction and deformable die. With the “rigid no heat conduction” type die, heat transfer from the environment and heat conduction within dies are ignored, meaning that dies’ temperature remains constant as the preset value. However, even with this die model, heat transfer in the workpiece is still considered during the simulation. There is no need to assign a material to rigid dies but, if this is the case, its thermal conductivity is used to determine the automatic heat transfer coefficient to the workpiece. For the B-pillar simulation, rigid type dies without heat conduction were considered, since the interest is focused on the stamped component and what happens to the dies is neglected.

Material data for this study were obtained using JMatPro version 11 software. Flow curves were obtained at 25°C and at temperatures between 50°C and 1050°C, with 50°C steps, at strain rates of 0.001, 0.01, 0.1, 1, 10, 100 and 1000 s⁻¹. In addition to density, defined thermal properties were

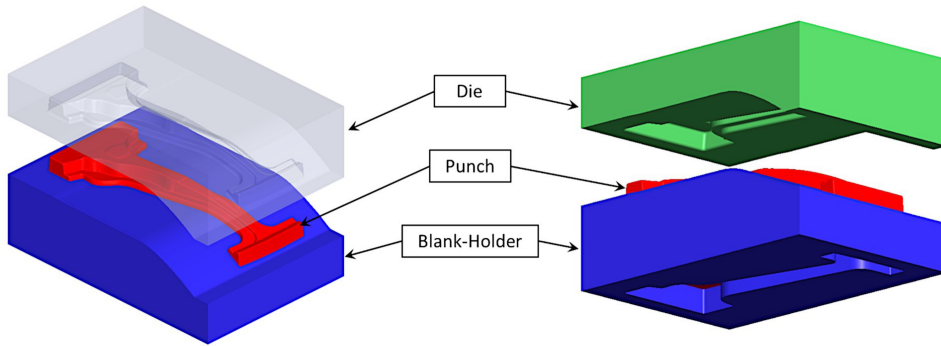


Figure 3. Tooling assembly for the simulation of the forming process.

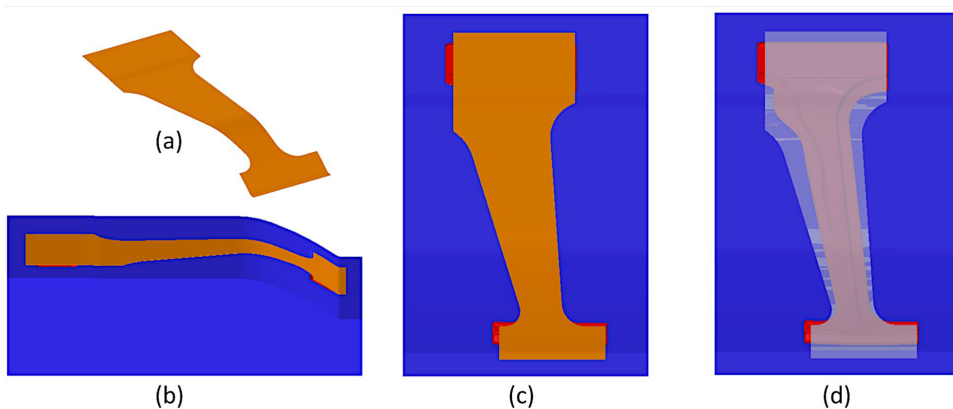


Figure 4. Blank shape used in the simulation (a), view of the deformed blank on the blank-holder (b), top view of the blank position on the blank-holder (c), and blank shape in relation to the punch (d).

thermal conductivity, specific heat capacity and thermal expansion coefficient. Defined mechanical properties were Young's modulus and Poisson's ratio, all varying from 25°C to 1050°C as well. Regarding the type of press machine, it was defined as a hydraulic system with a constant speed of 25 mm/s. Simufact software offers several types of press that can be assigned to simulations according to their objective and, for this work, hydraulics was chosen because it is the most commonly used in sheet forming. The choice of the forming speed was based on industrial processes already carried out with the same material. A constant friction coefficient of 0.3 was adopted, based on the work of Cui et al.³⁰. The initial blank temperature was assigned as 900°C according to Park et al.³², and the dies and room temperatures were assumed to be of 20°C. The heat transfer coefficient for the environment was defined as 50 W/m²K, according to Hu et al.³¹, and the heat transfer coefficient for the workpiece was set to "Automatic". In this mode, the software calculates the coefficient related to contact pressure and conductivity of the material, generating a variation curve. The initial mesh used in the blank was solid-shell hexahedral with a maximum size of 5 mm with 5 integration points in thickness, totaling 27,438 elements. A deformation remeshing condition was applied every 0.2 (20% strain). A closing die force on the blank-holder of 200 kN was also applied. This value was defined by trial and error to reach a value that

would not cause wrinkling. As we did not have the original FLD of this material to know if it would break, we assumed that it would not do so because the real piece did not fail, even if wrinkled; therefore, we focused on the minimum value. Finally, the displacement of the punch was assigned as the thickness of the sheet in between, i.e. the punch moved until it was 1.1 mm far from the die.

A second simulation was also performed, which corresponds to the heat extraction from the sheet with closed dies. In Simufact software, this step corresponds to a simulation called "cooling", into which results of the previous deformation step were imported. In this process, the time during which the sheet stays inside the dies was determined as 10 seconds, based on experiences from previous works and on the studies by Park et al.³², and Wang and Ma³³. All other previously determined parameters were kept constant.

2.3. RSW martensite tempering simulation

Provided that automotive parts are commonly joined by resistance spot welding (RSW), the martensitic tempering behavior in typical welding positions (regions 01, 02, 07, 08, 15 and 16 in Figure 1) was assessed via physical simulation. For the simulation, coupons with dimensions of 25 × 60 mm were cut from a second B-pillar, assumed to be identical to the one shown in Figure 1, with an abrasive cutting wheel. A thermal cycle corresponding to the one observed

in the SCHA3 was reproduced in a Gleeble® 540 physical simulator. Experiments were done using copper grips and K-type thermocouples spot-welded to the mid-length and mid-width of coupons. The free span between grips was of 20 mm. All experiments were carried out at ambient conditions, without vacuum. Compressed air with pressure of 100 psi ($\approx 7 \times 10^5$ Pa) was used as the cooling medium.

Thermal cycles were reproduced according to the work by Rezayat et al.³⁴. In the original work, these cycles were defined by finite element simulations in the SORPAS® software using the following parameters: compression time of 70 cycles ($\approx 1,197$ ms); two current pulses with duration of 12 cycles (≈ 200 ms), cooling time of two cycles (≈ 33 ms) and post-loading electrode retention time of 10 cycles (≈ 167 ms). Considering that regions with no statistically significant difference of hardness values were chosen, as will be seen ahead, three were heated to a target peak temperature of 580°C (regions 01, 02 and 07) and three to a temperature of 650°C (regions 08, 15 and 16).

2.4. Microstructural characterization

Samples described in **Section 2.1** were cut with an abrasive disk and embedded in bakelite for metallographic preparation. Thermally treated samples of **Section 2.3** were sectioned perpendicularly to their length, in the exact position where the thermocouple was welded, and mounted in the same manner. In all cases, the analyzed surface was the cross section of the sheet, parallel to the main direction of material flow during hot stamping. Conventional preparation was carried out using progressively finer SiC waterproof sandpapers, intermediate polishing with 6 μm and 1 μm diamond suspensions, and final polishing with a 0.3 μm alumina suspension. Samples were etched with Nital 2% (2 vol% nitric acid + 98 vol% ethanol) for microstructure reveal. Optical microscopy (OM) was carried out in an Axio Scope.A1 microscope equipped with an Axiocam ERc 5s camera. Scanning electron microscopy (SEM) using secondary electrons' signal (SE) was performed in a JSM-6510LV microscope with a tungsten filament, with an acceleration voltage of 20 kV, working distance of 12-13 mm and spot size SS50 (arbitrary unit).

2.5. Microhardness testing

Microhardness measurements were done in a HMV-2T E tester with a 1 kgf (9.8 N) load and a holding time of 10 s. Each sample was randomly indented five (05) times. Hereby presented results correspond to the respective average values and standard deviations.

2.6. Electrochemical tests

Potentiodynamic polarization tests were performed using a PGSTAT 128N potentiostat/galvanostat. Specimens were immersed in an electrolyte of saline solution containing 3.5% NaCl (m/V) and deionized water, and the electrochemical cell was composed of three electrodes: the electrode represented by the samples of interest, an Ag/AgCl reference electrode, and a platinum counter electrode.

Sample preparation followed the methodology already described in **Section 2.3**, with the additional step of welding a copper wire to samples before a cold resin embedding

procedure. Corrosion behavior on the cross section of the steel sheet was evaluated. Samples 01, 04, 12, 13, 15, 17 and 18 were tested. These samples were selected based on different microstructural constituents observed during metallographic analysis. Tests were performed considering five (05) repetitions for each sample, and the mean and standard deviation values were calculated.

Prior to the beginning of tests, the open circuit potential (OCP) was determined, characterized by a potential variation of less than 5 mV. The stabilization period was defined as 3600 s. After stabilizing the potential, the polarization test was started, with a scanning range from -1.0 to +0.2 V at a speed of 5 mV/s.

3. Results and Discussion

3.1. Numerical simulation

Strain distributions along the part at the end of the forming step are shown in Figure 5. It is possible to observe that, in general, deformation levels are relatively low, in the order of 7%, which corresponds to the bluish color of the image. This is natural to occur, since the part has mostly "U" bending strains, which usually result in low deformation values. However, certain regions exhibited considerably higher strain concentration, reaching levels around 45% (yellow color). In these regions, the forming behavior becomes of the deep drawing type, which explains these concentrations.

In terms of deformations observed in the Forming Limit Diagram (FLD), the same effects observed above occur, only with different numerical values. Figure 6 shows these values. This behavior is in accordance with other studies, such as those by Park et al.³² and Wang and Ma³³, in which the shape of the part was similar to the one studied in this paper.

3.2. Microstructure as affected by the hot stamping process

Optical microscopy images of some of the regions indicated in Figure 1 are shown in Figure 7. Nital etchant reveals ferrite and martensite in most carbon and low alloy steels and is also useful to reveal the microstructure of bainitic steels. Bramfitt and Benschoter³⁵ clarify that it etches ferritic grains and boundaries, and does not attack austenite. However, besides austenite, another microconstituent known as martensite-austenite (M-A), might also be present in these steels and appear as a non-etched structure³⁶. Due to the extreme refinement of the martensite in M-A, the structure usually appears as non-etched blocks, quite similar to pure austenite, being more easily distinguished by electron backscatter diffraction (EBSD)³⁷ or after a slight tempering treatment before etching³⁸. As can be seen, it is considerably difficult to distinguish different phases and microconstituents solely by optical microscopy. Nonetheless, an important information regarding chemical homogeneity can be drawn from optical micrographs: it is possible to observe the absence of microstructural banding, which results from chemical heterogeneities in the bulk of the material³⁹, showing that the austenitization treatment is adequate to homogenize the composition of the steel.

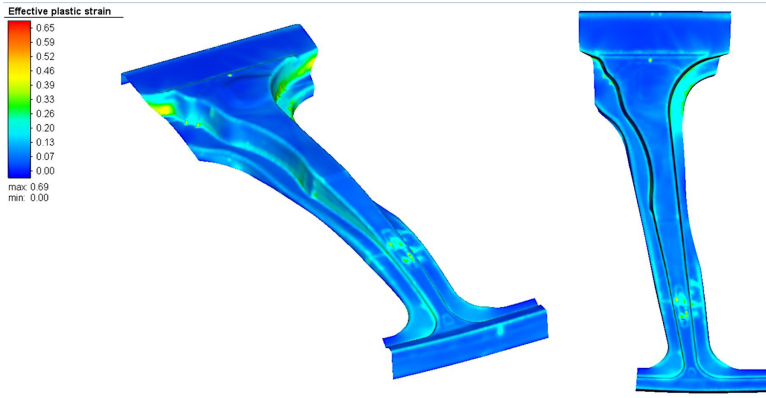


Figure 5. Effective strain distribution in the workpiece after the forming step.

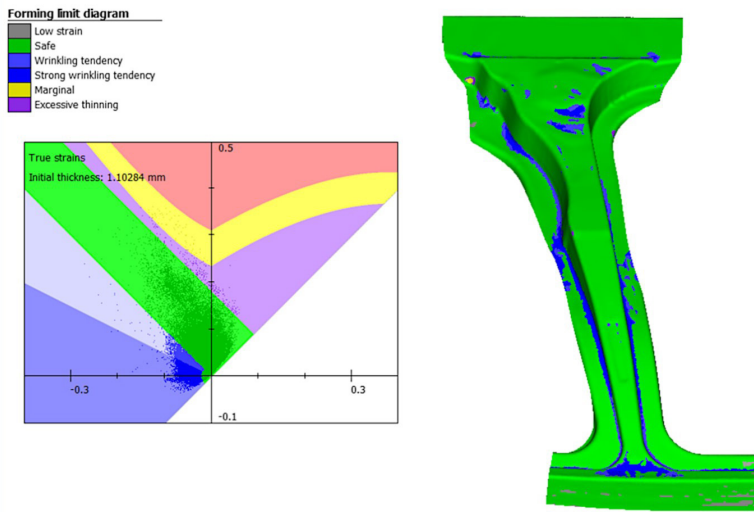


Figure 6. Forming Limit Diagram of the piece.

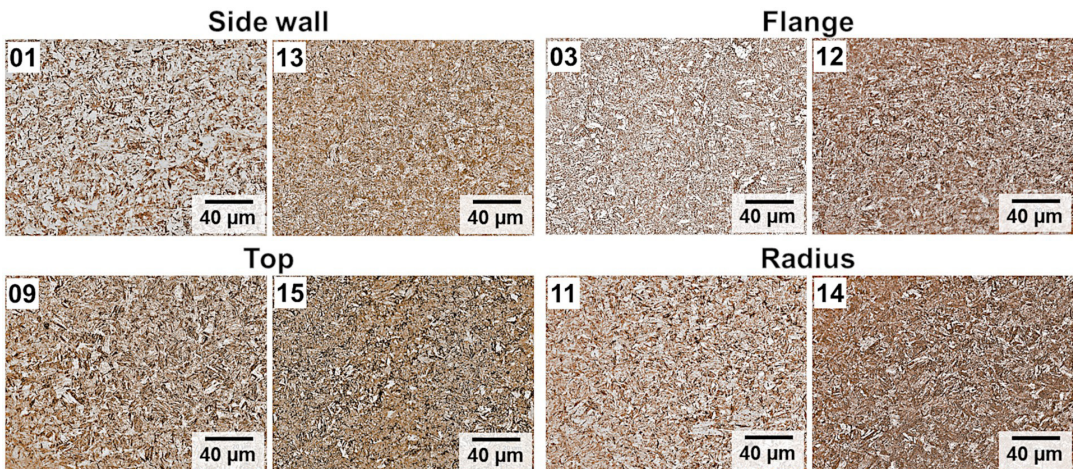


Figure 7. OM images showing the uniform microstructure of the B-pillar in different regions.

Average microhardness values of all regions are shown in Figure 8, along with their respective standard deviations. It can be noticed that values range from ~490 HV to ~540 HV.

Noteworthy are the minimum hardness levels shown by samples 12 (flange) and especially 18 (side wall), and the maximum levels observed in samples 4 (flange) and 5 (top).

Sample 12 is in a region where thickening takes place during deep drawing operations. Such thickening might be accompanied by a wrinkling of the sheet, which diminishes the effectiveness of heat extraction, due to the consequent formation of voids between the sheet and the die. Such phenomenon might also explain the similar behavior of sample 03. The location of sample 18, in its turn, undergoes intensive straining, leading to a detachment between sheet and die due to thinning, also hindering heat extraction. Overall, the hardness in all regions presents itself relatively high, in accordance with previously reported results for the 22MnB5 steel with different degrees of deformation and cooled at sufficiently high rates²¹.

A considerable dispersion of values is observed in Figure 8, especially considering the standard deviation bars. Comparing the four different sets of regions – side wall, flange, top and radius – it is not possible to distinguish specific hardness intervals belonging to each region, except for the radius region. To evaluate the statistical significance of the difference between averages, the Kruskal-Wallis test⁴⁰ was used for verification of the attendance of normal distribution requirement for the ANOVA (Analysis of Variance) test. In case of normal distribution ($P > 0.05$), the ANOVA analysis with the Tukey test is carried out; else, P values of pairwise comparisons were corrected according to the Bonferroni method⁴¹. The Kruskal-Wallis test provided a P value much lower than 0.05; therefore, the ANOVA was not employed. Bonferroni-corrected pairwise-compared P values show that samples 05, 12 and 18 differ most significantly from the rest; sample 18, particularly, does not differ significantly only from sample 12. Among all other samples, no significant difference exists, as shown by the employed method.

Figure 9 shows an approximated semi-hat profile comprising samples 12-15. Although a variation between different zones exist, the radius presents itself harder than the remaining regions. Statistical analysis shows that significant difference exists only between samples 12 (flange, softer) and 14 (radius, harder). As will be seen ahead, sample 12 presented an expressively ferritic microstructure, while sample 14 was mostly martensitic; sample 13 also presented a relatively high amount of ferrite, and sample 15, at last, was predominantly bainitic. Literature mostly reports side walls as the softest regions in Mn-B steels' hot-stamped parts^{6,8,9} while other studies report the top part as being softer⁴² or are unable to define a direct correlation between hardness and sample location due to high hardness fluctuations⁷. Studies developed in the cited works, however, were limited to simplified hat-shaped profiles. This means that microstructure and consequent hardness of the hot stamped material evolves in a rather complex fashion, relying on local deformation and cooling states that are strongly dependent on the component's geometry, thus reinforcing the importance of upscaling analyses to real components for enhanced robustness.

SEM images of different microstructures observed are shown in Figure 10, Figure 11 and Figure 12, along with the respective microhardness values. In Figure 13, higher magnification images are highlighted for exemplification of the encountered microconstituents. The main difficulty in the interpretation of SEM images lies on the complexity of the differentiation between bainitic and martensitic structures, as described by Navarro-López et al.³⁷ and Taylor

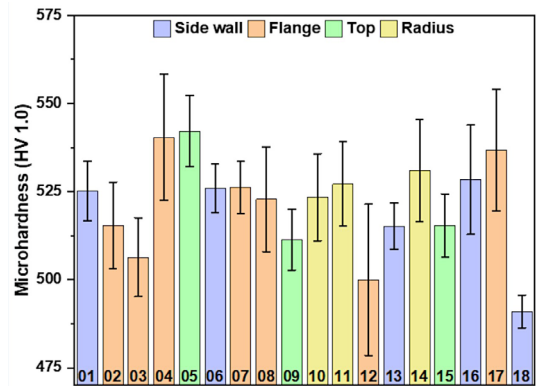


Figure 8. Average microhardness values obtained for all analyzed regions. Error bars correspond to the respective standard deviations.

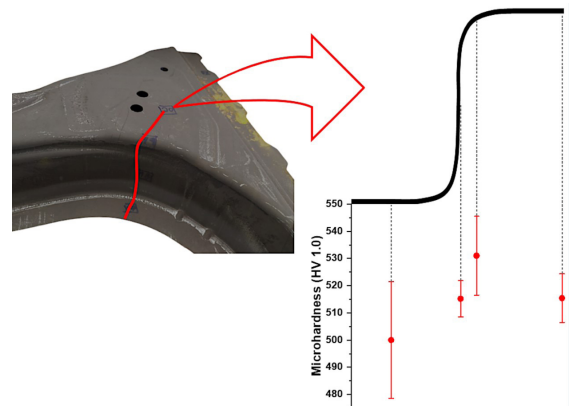


Figure 9. Semi-hat profile comprising samples 12-15 with the respective average microhardness values.

and McCulloch⁸. Ferrite identification is simpler, due to its morphology and the highest degree of surface relief caused by etching, while martensite and bainite present smaller degrees of relief. Likewise, Bhadeshia³⁶ points out and Navarro-López et al.³⁷ reinforce that retained austenite and M-A are easily distinguished by the lack of and lighter etching, respectively.

In side wall regions (Figure 10), it is possible to observe that sample 13 presents a significant amount of ferrite islands, while samples 01, 06 and 16 are predominantly martensitic. However, few ferritic structures were seen in samples 01 and 06. Sample 18 shows an expressive amount of ferrite, which justifies its minimum average hardness. Regarding top samples (Figure 11), 09 and 15 present a large amount of ferritic and bainitic structures, differently from sample 05. Again, nonetheless, a small amount of ferrite was observed in this region. With respect to radius samples (Figure 11), very little variation was observed between samples, with the refinement degree of the martensitic microstructure as the main difference. Finally, in flange regions (Figure 12), sample 12 contains a significant amount of ferrite. In all other samples, except for 04, ferritic zones in smaller amounts were detected. The presence of retained austenite was not directly

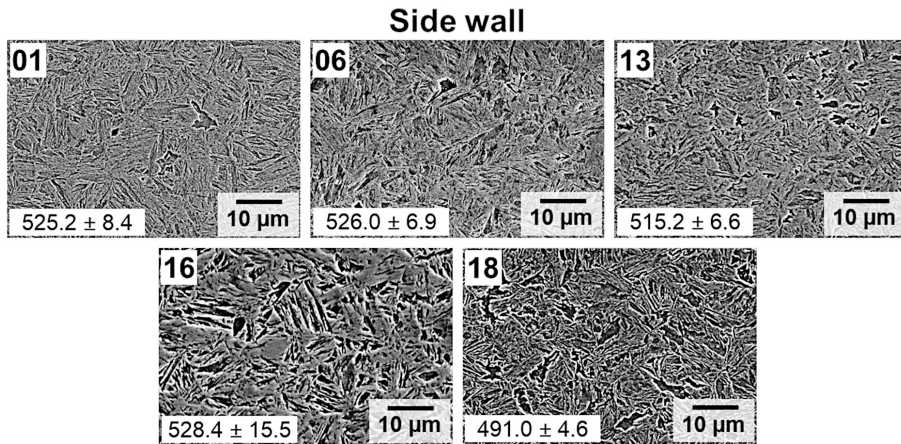


Figure 10. SE-SEM images of side wall samples.

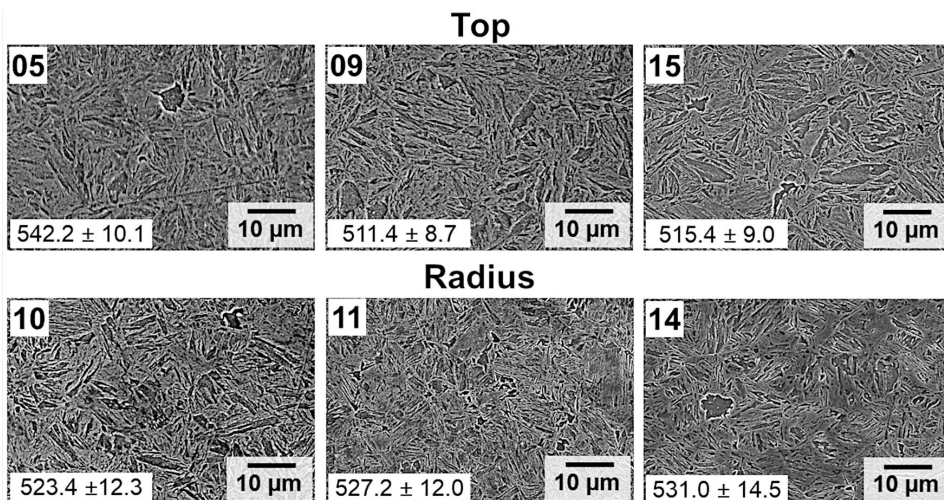


Figure 11. SE-SEM images of top and radius samples.

detected, except for regions where the M-A constituent was observed. Golem et al.⁴³ states that typically, the volume fraction of retained austenite in hot-stamped boron steels is no higher than 2%. In Figure 13, it is possible to notice the presence of coalesced martensite and bainite in samples 04, 13 and 15. These structures present themselves coarse and result from the coalescence of adjacent laths with identical crystallographic orientations. The negative effect these features exert in toughness have been extensively reported⁴⁴⁻⁴⁷.

In Figure 14 are shown the microstructures of two radius samples, 11 and 14, acquired from outer, central and inner regions of the corner. Cold bending has shown to impact the through-thickness microstructure of steels, due to the tensile strain state in outer regions, compressive strain state in inner regions and neutral state in the center, and such behavior has been thoroughly depicted in the literature⁴⁸⁻⁵¹. On the other hand, studies focused on the microstructural evolution during hot or warm sheet bending are scarce. One work on the assessment of the influence of hot rolling conditions on

the formation of ultra-fine grains in a 0.16% C – 0.2% Si – 1.4% Mn – 0.03% Nb steel, by Inoue et al.⁵², has shown that, when rolling takes place at temperatures well above A_{r3} , the microstructure is not sensitive to strain distribution through the sheet's thickness, while rolling at temperatures closer to A_{r3} causes a refinement variation from the surface to the center of the sheet. Therefore, the hot deformation at sufficiently high temperatures during stamping appears not to affect the microstructural distribution through the sheet's thickness.

Temperature and effective strain profiles obtained by numerical simulation for some locations of the hot-stamped B-pillar are shown in Figure 15. Results, yet approximated, due to the difficulty to obtain an exact correspondence between the analyzed locations in the simulated CAD part and in the real B-pillar, confirm that final microstructure does not depend solely on cooling rate, but also on deformation degree and temperature. In regions 04 and 05, for instance, simulated cooling rates were not as high; however, strain

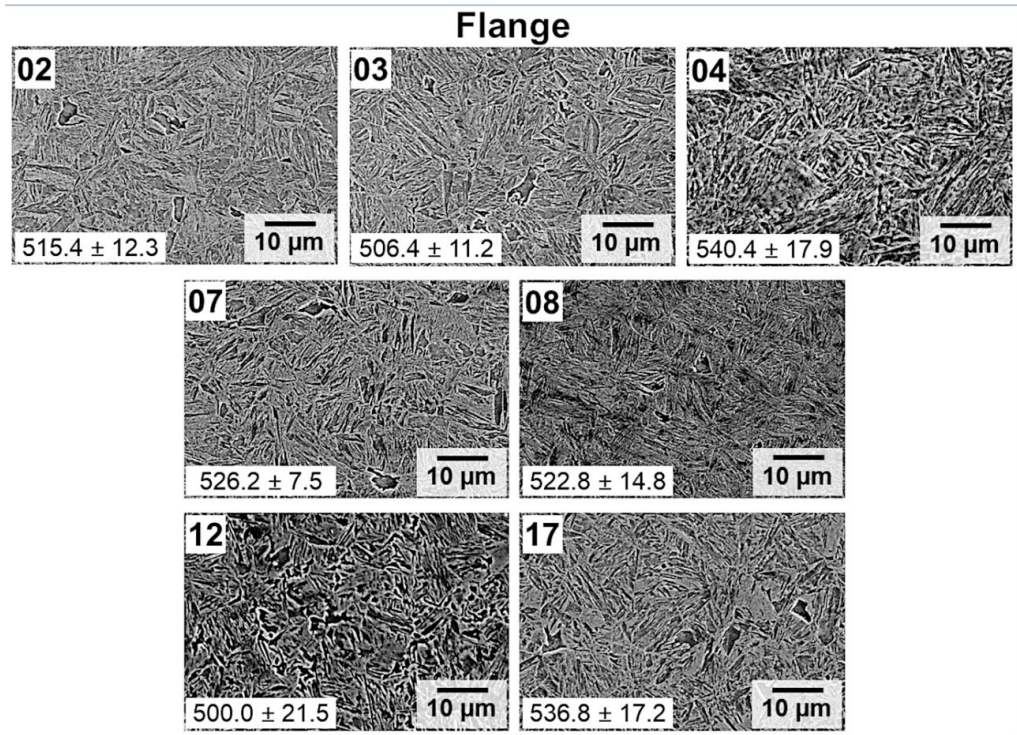


Figure 12. SE-SEM images of flange samples.

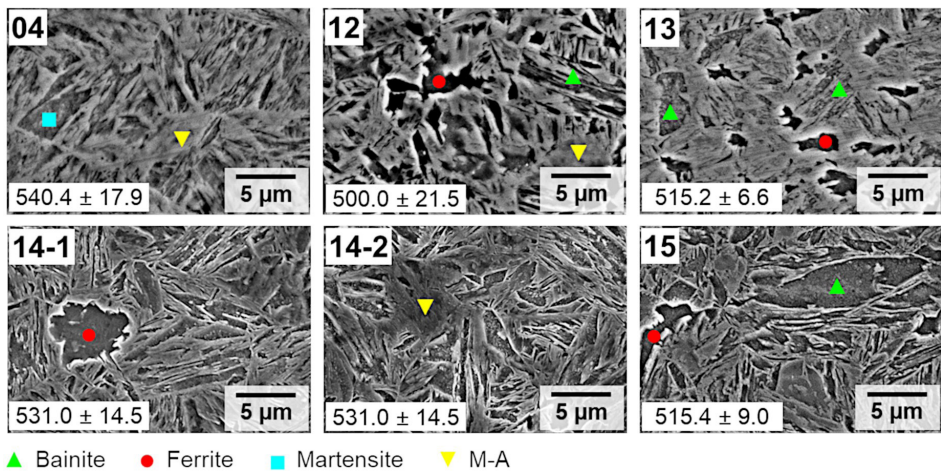


Figure 13. Higher magnification SE-SEM images for exemplification of some microstructural features observed.

levels in these locations were extremely low, showing that the low deformation was critical to minimize the occurrence of diffusive transformations, resulting in higher hardness values. In regions 12, 13 and 18, cooling rates were higher, but strain levels, on the other hand, were also expressive, suggesting the formation of deformation-induced ferritic and bainitic phases, resulting in significant hardness decrease. These findings are supported by previous works wherein austenite deformation promoted the formation of ferrite and bainite^{15,22,53,54}, and

increased the critical cooling rate necessary to achieve a fully martensitic microstructure⁵⁴. Nikravesh et al.²⁴ have derived continuous cooling transformation (CCT) diagrams for 22MnB5 with and without deformation, and evidenced the reduction of the incubation time for ferritic and bainitic transformations caused by deformation. Zhou et al.⁵⁴ further pointed out that, the higher the deformation temperature after austenitization, the more favored the martensitic microstructure due to recrystallization, given that deformation-induced

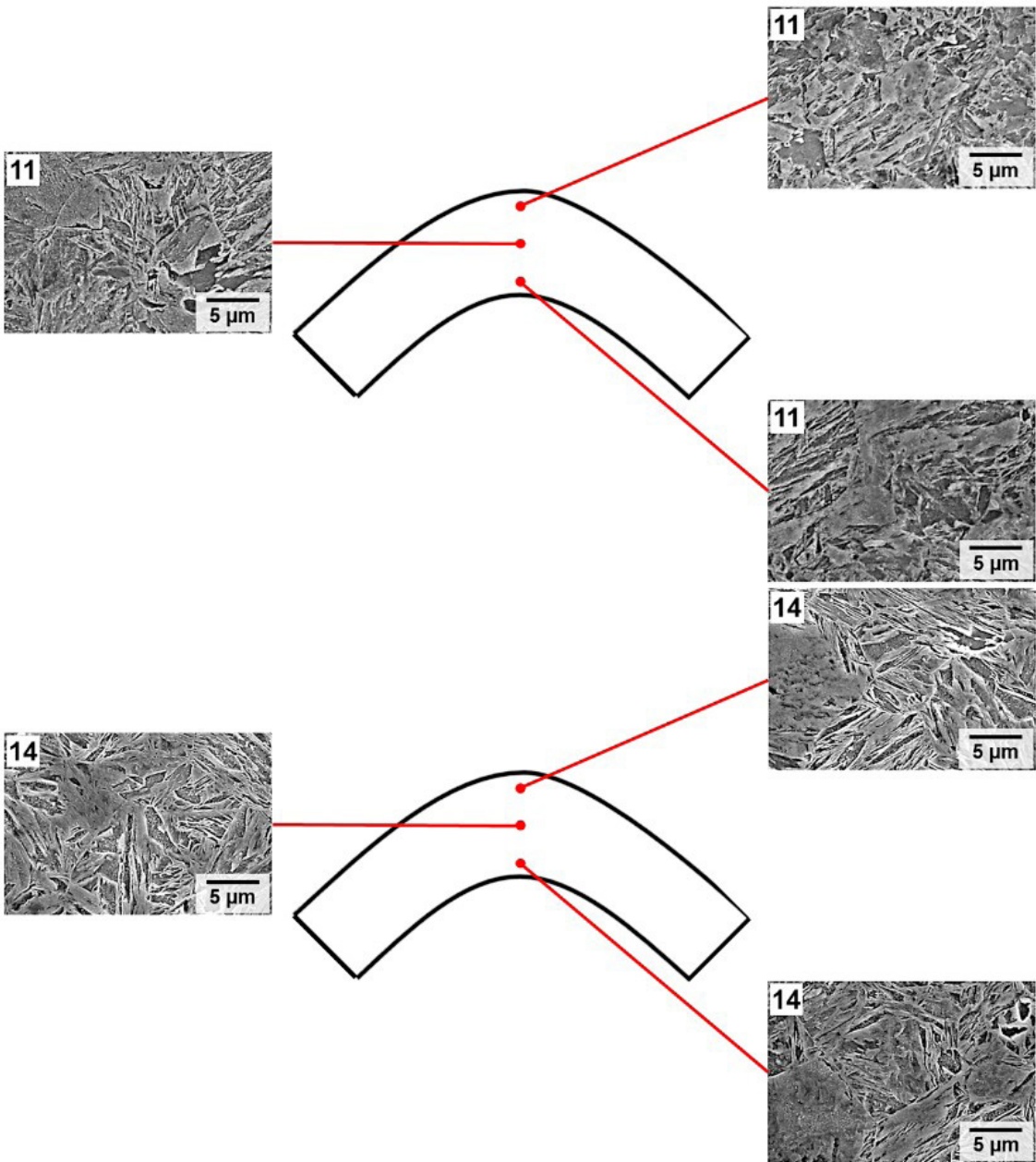


Figure 14. SE-SEM images of outer, central and inner regions of radius samples 11 and 14.

defects accelerate carbon diffusion and act as nucleation sites for diffusive transformations. Besides increasing the deformation temperature, increased strain rates and cooling rates are also important to suppress ferritic transformation, by decreasing the time available for nucleation and growth.

It is important to mention that the numerical simulation, regarding the interfacial heat transfer coefficient between part and tools (IHTC), is still not fully optimized, especially regarding coated materials. As shown by Hu et al.³¹ and Chang et al.⁵⁵, the IHTC is influenced by roughness of the sheet, contact pressure, sheet temperature and oxide layer, and these parameters may vary during the sheet forming

process. Thus, the temperature results of Figure 15a may still have discrepancies in relation to reality.

3.3. Electrochemical analysis

Figure 16a shows the linear polarization curves (LP) obtained from different regions of the B-pillar. It was not possible to directly interpret and extract parameters from the curves in terms of corrosion tendency. All samples presented similar characteristic curves, with stabilization at 6.9155 mA and -0.2 V, approximately. Besides, there was no evidence of passive behavior and localized corrosion in any of the samples. Based on the Tafel extrapolation,

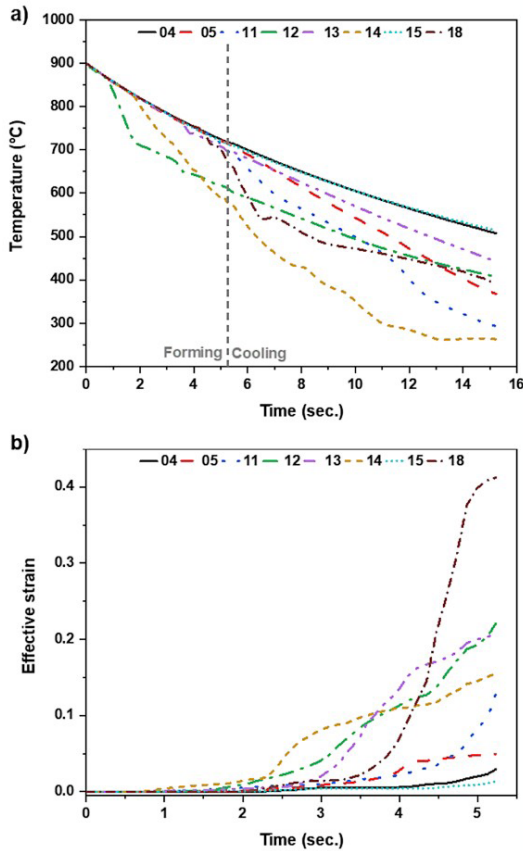


Figure 15. Temperature (a) and equivalent strain (b) curves drawn from the numerical simulation of the hot stamping process for some locations of the B-pillar workpiece according to Figure 1.

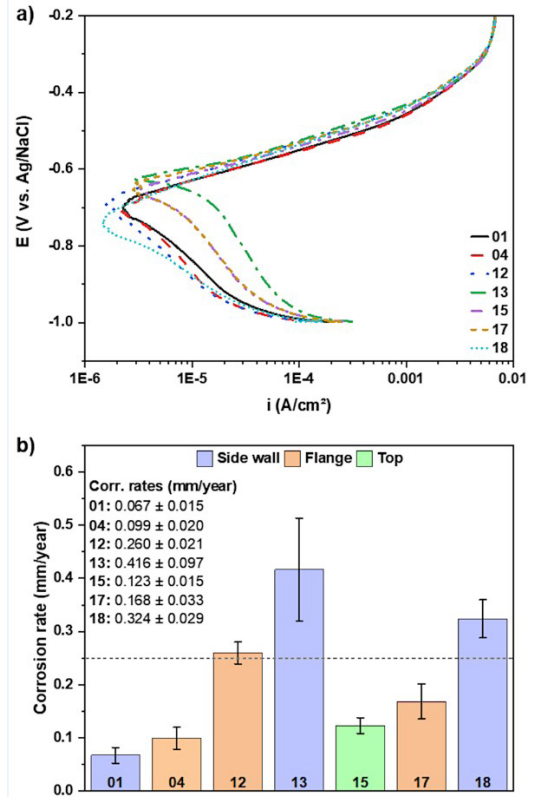


Figure 16. Polarization curves of different regions of the B-pillar according to Figure 1(a), and corrosion rates obtained from the different regions of the B-pillar (b). The dashed line indicates the NACE minimum threshold value that defines severe corrosion for steels in a 3.5 wt% NaCl solution (0.25 mm/year).

it was possible to determine the corrosion rate of the different regions, and results are presented in Figure 16b. The minimum threshold value defined by the U.S. National Association of Corrosion Engineers (NACE)⁵⁶ was also added to the figure as indicative of severe corrosion of steels in a 3.5 wt% NaCl solution. In this sense, it can be assumed that materials with a corrosion rate higher than 0.25 mm/year undergo severe corrosion, which is the case of samples 12, 13 and 18, although results from sample 13 showed a relatively high standard deviation as compared with the remaining samples.

Statistical analyses (ANOVA followed by Tukey test) were performed in these data, and it was found that samples 13 and 18 present superior corrosion rates, statistically equal to each other, while the corrosion rate of sample 12 is statistically smaller than those of samples 13 and 18 and superior to the rates shown by other samples. Samples 12, 13 and 18 showed the highest values because of the relatively large amounts of ferrite found in the microstructures, and ferrite is indeed acknowledged as the most susceptible phase to corrosion, i.e. the most anodic phase^{17-19,57}. In microconstituents containing carbides (bainite and pearlite), galvanic corrosion takes place, with preferential attack of ferritic regions. However, the formation of galvanic pairs does not necessarily lead to an increase in corrosion rate; on the contrary, in the works

by Neetu et al.¹⁷ and Moon et al.¹⁸, bainitic microstructures presented lower corrosion rates than ferritic ones. In the work by Katyiar et al.⁵⁷, bainitic microstructures presented even lower corrosion rates than martensite itself, while pearlitic and spheroidized microstructures were the ones with the lowest corrosion rates. On this basis, it was possible to infer that bainite does not play a decisive role in the increase of corrosion rates in the microstructure, and the single phase of interest in this regard is ferrite. Similarly, in the work by Katyiar et al.⁵⁷, differences between corrosion rates of martensitic and tempered martensitic structures were negligible, whereas Inam et al.¹⁹ were not able to obtain a linear correlation between corrosion rate and tempering time, with shorter tempering times (whose effect would be similar as that achieved by the employment of a lower tempering temperature) leading to an increase of corrosion rate and longer tempering times (similar to higher tempering temperatures) leading to a decrease of corrosion rate as compared with the fresh martensitic condition. These authors have all previously shown that ferrite is known to behave as an anode with respect to other phases, and its amount is critical to determine the corrosion severity of the alloy. The possibility of inclusion-related corrosion was disregarded because no inclusions were observed in the microstructure of the steel, neither by SEM nor by OM analyses.

3.4. RSW martensite tempering simulation

Temperature curves obtained during physical simulation of the SCHAZ are shown in Figure 17. The cooling rate obtained with compressed air cooling was much lower than the cooling rates usually experiences during RSW. The maximum cooling rate reached in the Gleeble® platform depends on several factors, e.g. thermal conductivities of the grips and of the tested material, specimen geometry and cooling medium. According to Lin⁵⁸, ambient air has a thermal conductivity lower than those of gases such as helium or hydrogen and, therefore, imposes lower cooling rates within the same conditions. In a work on the simulation of the HAZ of advanced steels in the same equipment, Dancette et al.¹¹ evidenced significant effects of quenching medium on the cooling rate. Nevertheless, in the present work, cooling rates of at least 50°C/s were verified down to temperatures as low as 200°C (Figure 17a), well above the reported critical cooling rates to suppress diffusive transformations in the 22MnB5 steel, that typically range between 25 and 40°C/s^{10,59}. Therefore, cycles were considered satisfactory for subsequent analyses.

Average microhardness values of all samples before and after physical simulation of the SCHAZ are shown in Table 2, together with the percent hardness decrease (with respect to the initial condition) and the peak temperature. Hardness decrease levels are in accordance with previous works³⁴. Variations of the peak temperature with respect to the target values of 580°C and 650°C can be noticed. Considering

that the same program was ran for all specimens belonging to each set of target temperature, factors such as specimen flatness, depending on the regions from which they were taken, specimen size variation, since they were roughly sectioned, likely reminiscence of the Al-Si coating, and variations in the reproduction of the grip + specimen assembly may be accounted for the lack of reproducibility. As previously mentioned, no significant difference between average hardness values in different regions existed before the application of the thermal cycle. Afterwards, all regions experienced an expressive hardness decrease. As expected, softening degree is directly related to the peak temperature, becoming higher as the peak temperature increases. Furthermore, a weaker tendency of increasing softening degree with the increase of the initial hardness is seen, which can be explained by a probable higher amount of martensite in the microstructure available for tempering. A similar effect was observed by Eller et al.^{60,61}, with the softening degree after tempering decreasing as the initial hardness of the base material decreased, i.e. as the bainite fraction increased. However, peak temperature clearly plays a more decisive role.

Ghassemi-Armaki et al.⁶² have shown that Gleeble® simulations produce results that are sufficiently representative of the HAZ of real welded joints, meaning that physical simulations constitute a powerful tool for the study of the weldability of materials and of the properties of welds. For 22MnB5 steel, minimum hardness levels of 295-300 HV were observed in the HAZ^{13,63,64}.

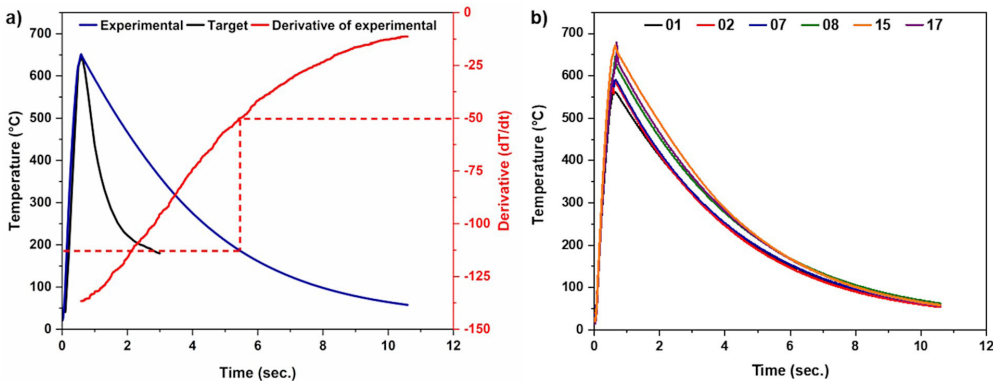


Figure 17. Resulting curves after the application of the simulated SCHAZ thermal cycle for some locations of the B-pillar workpiece according to Figure 1: comparison between experimental (obtained) and target curves (a), and the experimental curves obtained in each location (b).

Table 2. Average hardness values pre- and post-RSW SCHAZ simulation, with their respective standard deviations, as well as percent hardness decrease and reached peak temperatures.

Sample	Initial hardness (HV 1.0)	Final hardness (HV 1.0)	Hardness decrease (%)	Peak temperature (°C)
01	525.2 ± 8.4	324.0 ± 5.8	38.3	563
02	514.3 ± 12.3	333.6 ± 4.2	35.3	586
07	526.2 ± 7.5	322.0 ± 6.0	38.8	591
08	522.8 ± 14.8	312.0 ± 6.0	40.3	646
15	515.4 ± 9.0	303.0 ± 6.6	41.2	672
17	536.8 ± 17.2	308.4 ± 6.2	42.5	679

Microstructures of selected regions before the SCHAZ simulation, i.e., in the hot-stamped condition, and after, i.e., in the tempered condition, are shown in Figure 18, along with their average microhardness and respective standard deviations. In all hot-stamped microstructures, ferritic grains were observed, indicating the absence of a

fully martensitic in all regions. However, it can be said that microstructures were mostly martensitic. As shown by Lu et al.¹³, tempered martensite is morphologically defined by poorly-defined boundaries and a relatively coarse structure as compared with quenched martensite, in addition to the presence of carbides that precipitate as a result of carbon

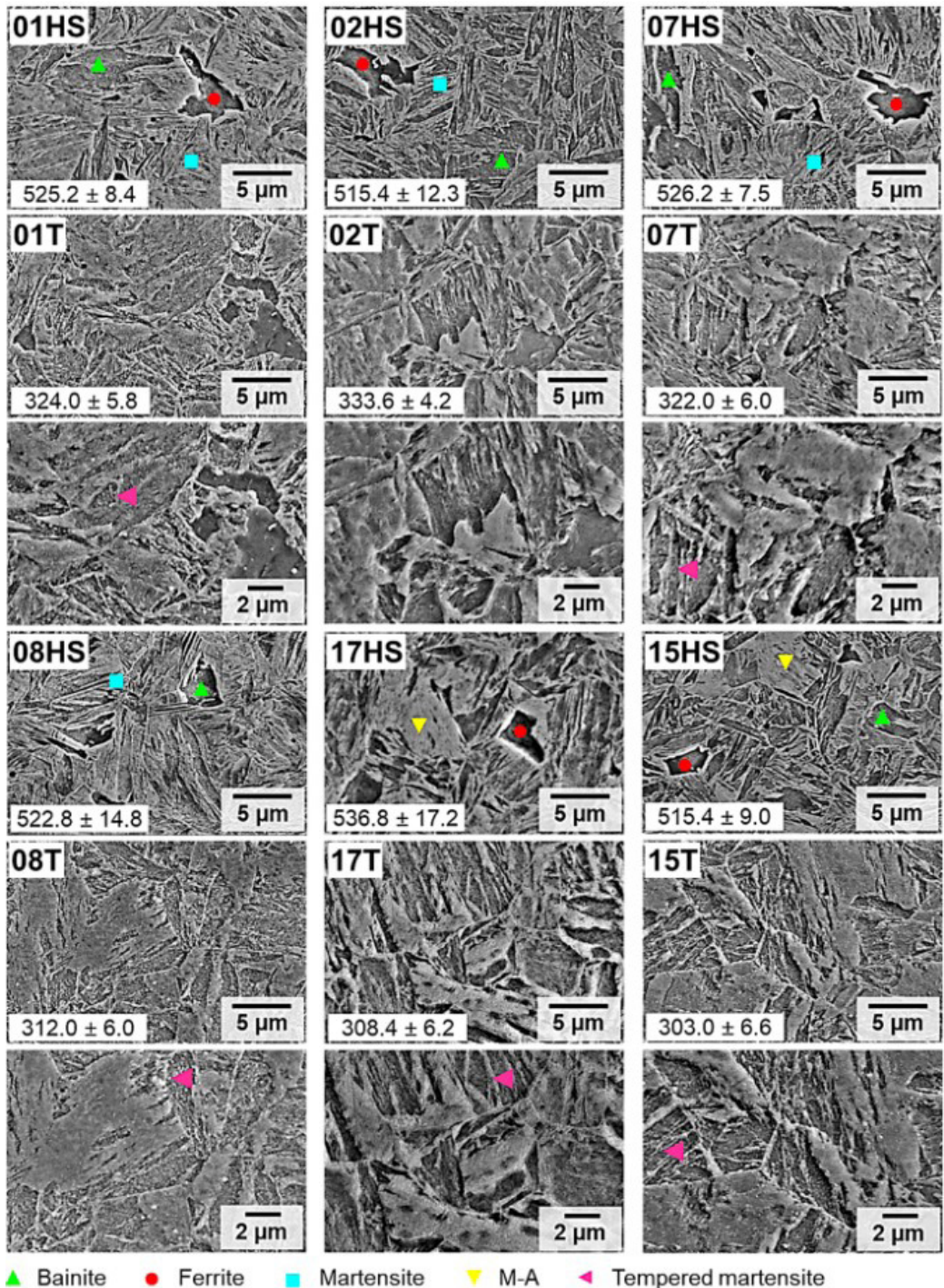


Figure 18. Microstructures pre- (HS: hot stamped) and post- (T: tempered) physical simulation of the SCHAZ of the RSW process. For tempered conditions, two magnifications are presented.

rejection, which can be easily seen in the form of fine white particles. Xu et al.⁵¹ associate these particles with carbides. Rezayat et al.³⁴ and Tamizi et al.⁶⁵ reported that tempering at higher temperatures leads to the formation of coarser carbides, especially in the form of films along the boundaries of martensitic substructures, while tempering at lower temperatures results in the precipitation of finer and more dispersed particles.

4. Conclusions

The microstructural evolution of a hot-stamped boron steel automotive B-pillar was analyzed and correlated with thermal cycle and effective strain data obtained by numerical simulation. In addition, the influence of this microstructural evolution on corrosion properties and martensitic tempering behavior was evaluated. The main findings can be summarized as follows:

- Numerical simulation by finite elements showed that, in general, hot stamping of the part resulted in low levels of deformation in FLD. However, in some sidewall and flange regions, higher levels of deformation were found (0.36 in major strain and 0.2 in minor strain). In these regions, the behavior becomes similar to the deep drawing type.
- Microstructural analysis showed that, in the assessed regions (side wall, flange, top and radius), the microstructure after hot stamping is hardly ever completely martensitic, but rather a complex martensite/bainite/ferrite mixture with various morphologies, resulting in hardness variation along the part. These results prove that the microstructure of the hot-stamped boron steel is strongly affected by the complex thermomechanical cycle encountered in certain zones, and not solely by the sheer fact of being a radius, top, wall or flange feature alone.
- Other relevant microstructural findings not usually reported for 22MnB5 include the presence of microconstituents as M-A and coalesced martensite/bainite, and the assessment of through-thickness microstructure variation in bending (radii) regions, showing that no relevant variation takes place in these conditions.
- Numerical simulation supported microstructural analysis results, showing that the final microstructure strongly depends on a combination of strain levels and cooling rates, which vary considerably along the part. Higher deformation was critical to maximize the occurrence of strain-induced ferritic transformations, resulting lower hardness values.
- Electrochemical analysis using Tafel extrapolation of polarization curves showed that regions with higher ferrite contents resulted in higher corrosion rates, since ferrite behaves as an anode and other microconstituents, such as bainite and martensite, are not regarded as critical when it comes to corrosion. Therefore, the strain level has a consequential great influence on the corrosive behavior of different regions within the part.
- Physical simulation of the SCHAZ showed that all regions experience a hardness decrease, as result

of martensite tempering. The softening degree was unrelated to the previous microstructure and directly related to the peak temperature (thermal cycle), becoming higher as peak temperature increases.

- These findings allow a better understanding of the behavior of 22MnB5 steel when subjected to real processing conditions, and how such behavior reflects on its compliance with subsequent application requirements. The methodology can be extended to other advanced steels, and currently available facilities for thermomechanical simulations provide grounds for macroscale replication of specific thermal and strain conditions, meaning that a deeper evaluation of the material's processing conditions on properties such as tensile strength and ductility and impact toughness can be done.

5. Acknowledgments

The authors would like to acknowledge Ford Motor Company Brazil and SENAI DN (National Department) for the financial support through the Rota 2030 program (project 329785). Additionally, the authors acknowledge the company Magna Cosma (Brazil) for supplying the B-pillar workpieces and the alliance created for the development of the project.

6. References

1. Giampieri A, Ling-Chin J, Ma Z, Smallbone A, Roskilly AP. A review of the current automotive manufacturing practice from an energy perspective. *Appl Energy*. 2020;261:114074.
2. Rana R, Singh SB, editors. *Automotive steels: design, metallurgy, processing and applications*. Duxford: Woodhead Publishing; 2017. 469 p.
3. Karbasian H, Tekkaya AE. A review on hot stamping. *J Mater Process Technol*. 2010;210:2103-18.
4. Westermann H, Reitz A, Mahnken R, Schaper M, Grydin O. Microstructure transformations in a press hardening steel during tailored thermo-mechanical processing. *Steel Res Int*. 2021;93(1):2100346.
5. Reitz A, Grydin O, Schaper M. Influence of thermomechanical processing on the microstructural and mechanical properties of steel 22MnB5. *Mater Sci Eng A*. 2022;838:142780.
6. Li Y, Li S. Deep learning based phase transformation model for the prediction of microstructure and mechanical properties of hot-stamped parts. *Int J Mech Sci*. 2022;220:107134.
7. Naderi M, Ketabchi M, Abbasi M, Bleck W. Analysis of microstructure and mechanical properties of different hot stamped B-bearing steels. *Steel Res Int*. 2010;81(3):216-23.
8. Taylor T, McCulloch J. Effect of part/die boundary conditions on microstructural evolution during hot stamping 2000 MPa class boron steel. *Steel Res Int*. 2018;89:1700495.
9. Grydin O, Andreiev A, Holzweißig MJ, Rüsing CJ, Duschik K, Frolov Y et al. Short austenitization treatment with subsequent press hardening: correlation between process parameters, microstructure and mechanical properties. *Mater Sci Eng A*. 2019;749:176-95.
10. Naderi M, Saeed-Akbari A, Bleck W. The effects of non-isothermal deformation on martensitic transformation in 22MnB5 steel. *Mater Sci Eng A*. 2008;487:445-55.
11. Dancette S, Massardier-Jourdan V, Fabrègue D, Merlin J, Dupuy T, Bouzekri M. HAZ microstructures and local mechanical properties of high strength steels resistance spot welds. *ISIJ Int*. 2011;51(1):99-107.

12. Shi L, Alexandratos SA, O'Dowd NP. Prediction of prior austenite grain growth in the heat-affected zone of a martensitic steel during welding. *Int J Press Vessels Piping*. 2018;166:94-106.
13. Lu Y, Peer A, Abke T, Kimchi M, Zhang W. Subcritical heat affected zone softening in hot-stamped boron steel during resistance spot welding. *Mater Des*. 2018;155:170-84.
14. Levander L. Improved scale adhesion of uncoated hot stamped steel. In: 3rd International Conference on Advanced High Strength Steel and Press Hardening (ICHSSU2016); 2016 Aug 25-27; Xi'an. Proceedings. New Jersey: World Scientific; 2017. p. 26-30.
15. Fan DW, Kim HS, Cooman BC. A review of the physical metallurgy related to the hot press forming of advanced high strength steel. *Steel Res Int*. 2009;80(3):241-8.
16. Couto CP, Revilla RI, Colosio MA, Costa I, Panossian Z, Graeve I et al. Electrochemical behaviour of 22MnB5 steel coated with hot-dip Al-Si before and after hot-stamping process investigated by means of scanning Kelvin probe microscopy. *Corros Sci*. 2020;174:108811.
17. Neetu, Katiyar PK, Sangal S, Mondal K. Effect of various phase fraction of bainite, intercritical ferrite, retained austenite and pearlite on the corrosion behavior of multiphase steels. *Corros Sci*. 2021;178:109043.
18. Moon AP, Sekhar KC, Mahanty S, Sangal S, Mondal K. Corrosion behavior of newly developed high-strength bainitic railway wheel steels. *J Mater Eng Perform*. 2020;29(5):3443-59.
19. Inam A, Imtiaz Y, Hafeez MA, Munir S, Ali Z, Ishtiaq M et al. Effect of tempering time on microstructure, mechanical, and electrochemical properties of quenched-partitioned-tempered Advanced High Strength Steel (AHSS). *Mater Res Express*. 2019;6(12):126509.
20. Zhao Z, Zhao P, Cheng H, Lu X, Miao J, Chen Y et al. Investigation of influence of microstructure on FH32 steel corrosion properties using Gleeble simulation of heat-affected zone and electrochemical methods. *Int J Electrochem Sci*. 2019;14:9948-59.
21. Barcellona A, Palmeri D. Effect of plastic hot deformation on the hardness and continuous cooling transformations of 22MnB5 microalloyed boron steel. *Metall Mater Trans, A Phys Metall Mater Sci*. 2009;40:1160-74.
22. Min J, Lin J, Min Y. Effect of thermo-mechanical process on the microstructure and secondary-deformation behavior of 22MnB5 steels. *J Mater Process Technol*. 2013;213:818-25.
23. Zhu L, Gu Z, Xu H, Lü Y, Chao J. Modeling of microstructure evolution in 22MnB5 steel during hot stamping. *J Iron Steel Res Int*. 2014;21(2):197-201.
24. Nikravesh M, Naderi M, Akbari GH, Bleck W. Phase transformations in a simulated hot stamping process of the boron bearing steel. *Mater Des*. 2015;84:18-24.
25. Chen Y, Zhang H, Tang JJ, Han X, Cui Z. Integrated modelling of microstructure evolution and mechanical properties prediction for Q&P hot stamping process of ultra-high strength steel. *Chin J Mech Eng*. 2020;33:45.
26. Hu K, Zhou S, Han R, Gao J, Yang Y. Microstructure evolution and simulation in 22MnB5 steel during hot stamping. *J Mater Sci Chem Eng*. 2018;6:9-14.
27. Afkhami S, Javaheri V, Amraei M, Skriko T, Piili H, Zhao X et al. Thermomechanical simulation of the heat-affected zones in welded ultra-high strength steels: microstructure and mechanical properties. *Mater Des*. 2021;213:110336.
28. Baltazar-Hernández VH, Nayak SS, Zhou Y. Tempering of martensite in dual-phase steels and its effects on softening behavior. *Metall Mater Trans, A Phys Metall Mater Sci*. 2011;42(10):3115-29.
29. Dong Y, Qi XY, Du L, Yan L, Misra RDK. Effect of welding thermal cycle on microstructural characteristics and toughness in simulated heat affected zone of low-C medium-Mn high strength steel. *J Mater Eng Perform*. 2022;31(4):2653-63.
30. Cui J, Sun G, Xu J, Huang X, Li G. A method to evaluate the formability of high-strength steel in hot stamping. *Mater Des*. 2015;77:95-109.
31. Hu P, Ying L, Li Y, Liao Z. Effect of oxide scale on temperature-dependent interfacial heat transfer in hot stamping process. *J Mater Process Technol*. 2013;213:1475-83.
32. Park MK, Son HS, Kim TH, Choi BK. Formability, flow and heat transfer simulation of hot press forming B-pillar part and tools. In: 10th International Conference on Numerical Methods in Industrial Forming Processes Dedicated to Professor O. C. Zienkiewicz (1921–2009); 2010 Jun 13-17; Pohang. Proceedings. College Park: American Institute of Physics; 2010. p. 344-7.
33. Wang W, Ma JL. Hot stamping simulation with PAM-STAMP of the B-pillar of a well-known SUV. *Adv Mat Res*. 2015;1063:268-71.
34. Rezayat H, Ghassemi-Armaki H, Bhat SP, Sriram S, Babu SS. Constitutive properties and plastic instabilities in the heat-affected zones of advanced high-strength steel spot welds. *J Mater Sci*. 2019;54:5825-43.
35. Bramfitt BL, Benscoter AO. *Metallographer's guide: practices and procedures for irons and steels*. Materials Park: ASM International; 2002. 354 p.
36. Bhadeshia HKDH. About calculating the characteristics of the martensite-austenite constituent. In: International Seminar on Welding of High Strength Pipeline Steels; 2011 Nov 27-30; Araxá. Proceedings. Araxá: Companhia Brasileira de Metalurgia e Mineração (CBMM); 2013. p. 99-106.
37. Navarro-López A, Hidalgo J, Sietsma J, Santofimia MJ. Characterization of bainitic/martensitic structures formed in isothermal treatments below the Ms temperature. *Mater Charact*. 2017;128:248-56.
38. Girault E, Jacques P, Harlet P, Mols K, Van Humbeeck J, Aernoudt E et al. Metallographic methods for revealing the multiphase microstructure of TRIP-assisted steels. *Mater Charact*. 1998;40:111-8.
39. Krauss G. Solidification, segregation, and banding in carbon and alloy steels. *Metall Mater Trans, B, Process Metall Mater Proc Sci*. 2003;34(12):781-92.
40. Kruskal WH, Wallis WA. Use of ranks in one-criterion variance analysis. *J Am Stat Assoc*. 1952;47(260):583-621.
41. Bonferroni CE. Teoria statistica delle classi e calcolo delle probabilità. *Ist Super di Sci Econ Commer Firenze*. 1936;8:3-62.
42. Ying L, Hu P, Zhao X, Shi DY, Dai MH, Yu HY et al. Research on rapid-cooling press hardening process and its effect for formability of ultra high strength steel. In: 11th International Conference on Numerical Methods in Industrial Forming Processes: Numiform 2013; 2013 Jul 6-10; Shenyang. Proceedings. College Park: American Institute of Physics; 2013. p. 414-20.
43. Golem L, Cho L, Speer JG, Findley KO. Influence of austenitizing parameters on microstructure and mechanical properties of Al-Si coated press hardened steel. *Mater Des*. 2019;172:107707.
44. Bhadeshia HKDH, Keehan E, Karlsson L, Andréon HO. Coalesced bainite. *Trans Indian Inst Met*. 2006 [cited 2023 Apr 23];59(5):689-94. <https://www.phase-trans.msm.cam.ac.uk/2007/coalesced.pdf>
45. Pak JH, Bhadeshia HKDH, Karlsson L, Keehan E. Coalesced bainite by isothermal transformation of reheated weld metal. *Sci Technol Weld Join*. 2008;13(7):593-7.
46. Pak JH, Bhadeshia HKDH, Karlsson L. Mechanism of misorientation development within coalesced martensite. *Mater Sci Technol*. 2012;28(8):918-23.
47. Pous-Romero H, Bhadeshia H. Coalesced martensite in pressure vessel steels. *J Press Vessel Technol*. 2014;136:031402.
48. Miller CA, Neogi P. *Interfacial phenomena: equilibrium and dynamic effects*. 2nd ed. Boca Raton: CRC Press; 2008. 501 p. (Surfactant Science; 139).
49. Soomro IA, Pedapati SR, Awang M. Optimization of postweld tempering pulse parameters for maximum load bearing and

- failure energy absorption in dual phase (DP590) steel resistance spot welds. *Mater Sci Eng A*. 2021;803:140713.
50. Su YH, Oikawa K, Shinohara T, Kai T, Hiroi K, Harjo S et al. Time-of-flight neutron transmission imaging of martensite transformation in bent plates of a Fe-25Ni-0.4C alloy. *Phys Procedia*. 2017;88:42-9.
 51. Xu Y, Ji Q, Yang G, Bao S, Zhao G, Miao X et al. Effect of cooling path on microstructures and hardness of hot-stamped steel. *Metals*. 2020;10(12):1692.
 52. Inoue T, Qiu H, Ueji R. Through-thickness microstructure and strain distribution in steel sheets rolled in a large-diameter rolling process. *Metals*. 2020;10:91.
 53. Min J, Lin J, Min Y, Li F. On the ferrite and bainite transformation in isothermally deformed 22MnB5 steels. *Mater Sci Eng A*. 2012;550:375-87.
 54. Zhou J, Wang B, Huang M, Cui D. Effect of hot stamping parameters on the mechanical properties and microstructure of cold-rolled 22MnB5 steel strips. *Int J Miner Metall Mater*. 2014;21(6):544-55.
 55. Chang Y, Tang X, Zhao K, Hu P, Wu Y. Investigation of the factors influencing the interfacial heat transfer coefficient in hot stamping. *J Mater Process Technol*. 2016;228:25-33.
 56. Nace International: National Association of Corrosion Engineers. NACE publication 3D170 (latest revision): electrical and electrochemical methods for determining corrosion rates. Houston: National Association of Corrosion Engineers; 1984.
 57. Katiyar PK, Misra S, Mondal K. Comparative corrosion behavior of five microstructures (pearlite, bainite, spheroidized, martensite, and tempered martensite) made from a high carbon steel. *Metall Mater Trans, A Phys Metall Mater Sci*. 2019;50(3):1489-501.
 58. Lin M. Gas quenching with air products' rapid gas quenching gas mixture. Lehigh Valley: Air Products and Chemicals, Inc; 2007.
 59. Mohrbacher H. Martensitic automotive steel sheet - fundamentals and metallurgical optimization strategies. *Adv Mat Res*. 2015;1063:130-42.
 60. Eller TK, Greve L, Andres M, Medricky M, Meinders VT, Van Den Boogaard AH. Determination of strain hardening parameters of tailor hardened boron steel up to high strains using inverse FEM optimization and strain field matching. *J Mater Process Technol*. 2016;228:43-58.
 61. Eller TK, Greve L, Andres M, Medricky M, Geijselaers HJM, Meinders VT et al. Plasticity and fracture modeling of the heat-affected zone in resistance spot welded tailor hardened boron steel. *J Mater Process Technol*. 2016;234:309-22.
 62. Ghassemi-Armaki H, Biro E, Sadagopan S. Advanced characterization of HAZ softening of AHSS for crash modeling. *ISIJ Int*. 2017;57(8):1451-60.
 63. Ghassemi-Armaki H, Khan Q, Gill AS, Zilincik S. Characterization and modeling of spot-weld joints in press hardening steels associated with softening in heat affected zone. In: 11th European LS-DYNA Conference 2017; 2017 May 9-11; Salzburg. Proceedings. Dublin, USA: DYNAmore Corporation; 2017. p. 1-13.
 64. Qiao Z, Li H, Li L, Ran X, Feng L. Microstructure and properties of spot welded joints of hot-stamped ultra-high strength steel used for automotive body structures. *Metals*. 2019;9(3):285.
 65. Tamizi M, Pouranvari M, Movahedi M. Welding metallurgy of martensitic advanced high strength steels during resistance spot welding. *Sci Technol Weld Join*. 2017;22(4):327-35.